Resistance Spot Welds of 304l Austenitic Stainless Steel, Part 2 : Signals Measurement, Dynamic Resistance, Electrically Generated Forging Force, Metallurgy and Hardness Distribution Analysis

Nachimani Charde

Department of Mechanical Engineering, Faculty of Engineering, University Malaya, Malaysia
E-mail : nachicharde@yahoo.com

ABSTRACT

Part 1 of this research introduces the spot welds growth on 304L stainless steel; primarily supported by information such as the chemical property, specimen size, calculated-static resistance, welding lobe, welding schedule, simulation, tensile shear load, indentation, failure mode, and also the elongation during tensile test. In part 2, the analysis is furthered to understand the dynamic resistances, force profiles, electrically generated forging forces, macro and micro structural orientation and also the hardness distribution. Heat development during the welding process is proportionally influenced by the dynamic resistances and therefore several detailed analytical approaches have been included to understand the process variables certainly. Literally the dynamic resistances are proportionally related for the welding current and welding time changes but reversely behaved for the electrode force changes within the welding lobe limits. These resistive changes became the root cause of weld growth pertaining to heat variations. So the computations have been carried out from the perspective of welding current against the terminal voltage. On the other end, the force profiles are relatively measured to observe the electrode force variation with respect to the welding current changes. With the changes of process variables, the corresponding weld growth is analysed in terms of dynamic resistances in this experiment. Eventually the micro structural changes show the enrichment of coarsened grains but transformed in phases as results; which lead to slight increment of hardness at the welded areas as Rockwell hardness proves these increments as well.

Keywords : Signal measurement, Dynamic resistance, Macro and Microstructure, Hardness Distribution.

1.0 INTRODUCTION

Spot weld growths are usually expounded from its nugget growth and the bounding strength as how the results have been revealed in part 1 [1]. However, other parameters such as the heat generation that subjected to resistive changes, force variations during the welding sequence, and the solidification process that changes the macro and micro structural orientation are also important data to understand the weld growth deeply [2, 3]. In this paper, such parameters are investigated for each and every mille seconds during the welding process is going on. Besides a newly formulated approach for the computation of force changes becomes the breakthrough in this analysis; as it paves the mathematical formulation for the force changes in any spot welder.

2.0 EXPERIMENTATION

The base metals were welded as lap joints, having a dimension of 200 mm x 25 mm x 1 mm. The entire welding processes have been done using ordinary pneumatic based electrode actuation system, 75 kVA, AC-waveform spot welder [4]. A weld schedule for the signal capturing conditions is developed and listed in **Table 1.** The process signals are captured for three levels of

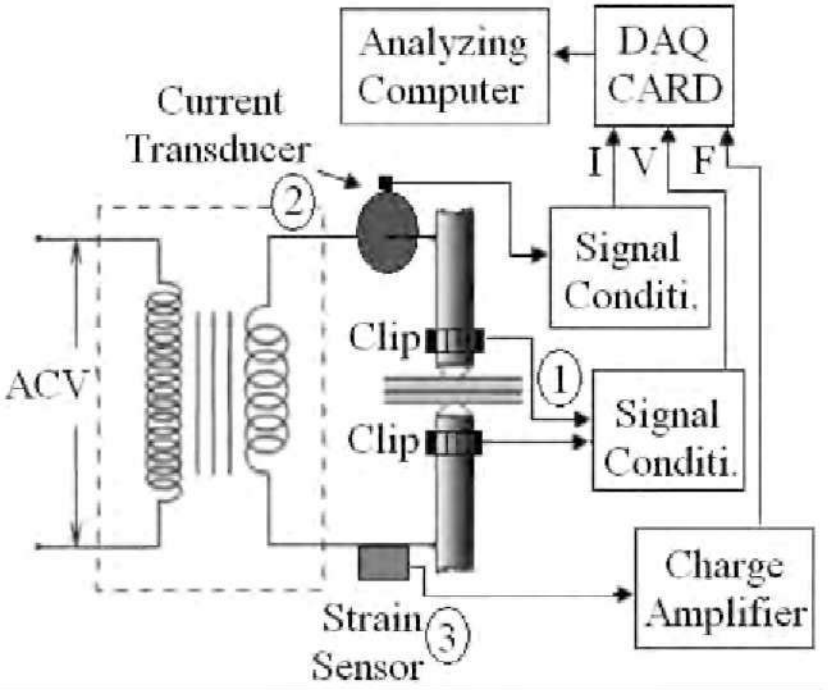

Fig. 1 : The instrumentation set up

Table 1 : Schedule for Electrical Signal, Forging Forces and Proportional Factor

Welding current (I) in kA	Weld time (t) In cycle	Squeezing force (F) in kN	Forging force from captured signals (F_g) in kN	Proportional Factor ($k = F_g/ItF_{(Squeeze)}$)
6	10 (0.2 S)	3	1.4	388.88×10^{-6}
7			2	476.19×10^{-6}
8			2.4	500.00×10^{-6}
6	10	3	1.4	388.88×10^{-6}
		4.5	1.45	268.51×10^{-6}
		6	1.52	211.11×10^{-6}
6	15 (0.3 S)	3	1.6	296.29×10^{-6}
7			2.1	333.33×10^{-6}
8			2.6	361.11×10^{-6}
6	15	3	1.58	292.59×10^{-6}
		4.5	1.64	202.46×10^{-6}
		6	1.60	148.14×10^{-6}
6	20 (0.4 S)	3	1.7	236.11×10^{-6}
7			2.1	250.00×10^{-6}
8			2.3	239.58×10^{-6}
6	20	3	1.72	238.88×10^{-6}
		4.5	1.75	162.03×10^{-6}
		6	1.80	125.00×10^{-6}

welding current (6, 7, and 8 kA), electrode pressing force (3, 4.5, 6 kN) and weld duration (10, 15 and 20 Cycle) in accordance with the welding lobes that presented in part 1. **Fig. 1** shows the instrumentation set up for process parameters' measurement. The process parameters signals (current, voltage and force) are captured using sensors, transducers, and crocodile clips [5]. The captured signals are then sent through conditioning and amplifying circuits to data analysing software (Labviews' Signal Express) from which the corresponding dynamic resistive patterns and the force profiles are plotted for practical cases [6, 7].

3.0 RESULTS AND DISCUSSION

Computation of Captured Signals

Fig. 2 was obtained from real force profile of pneumatic based spot welder for stainless steel. The squeezing profile (1) is the transient states at which the electrode pressing force (squeezed force) was achieved according to the pre-set value. Once it reached the pre-set values, it held the electrode with that particular force thereafter. If the present value of electrode pressing force is 3 kN for an instance, the pneumatic system will press the electrode lever to produce 3 kN and the welding current will be released then. The flow of huge amount of current causes vibration due to atomic breaks and releases acoustics waves relatively. So the vibration is coexisted in the force profile as an electrically generated forging force during the welding process. These forging forces play significant role as it determines the quality of the weld joints by escalating the electrode force. **Fig. 3** and **4** are showing the current and voltage waveforms that captured from this instrumental setup which was used to calculated the dynamic resistances respectively. The dynamic resistance is basically calculated from the terminal voltage and the real current flow (R=V/I).

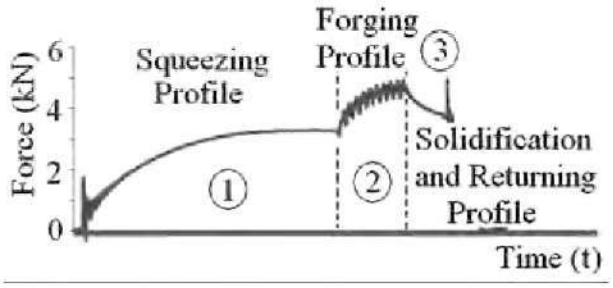

Fig. 2 : Force profile of pneumatic based spot welder for stainless steel

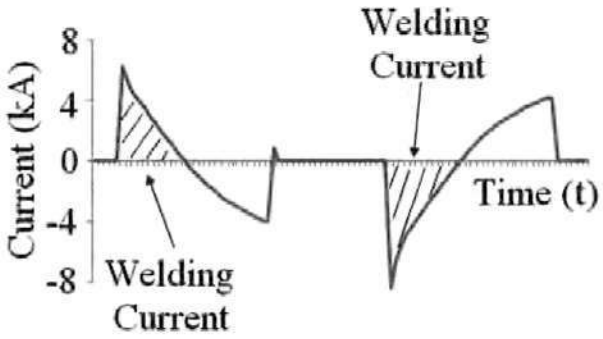

Fig. 3 : Current waveform from conditioning circuit

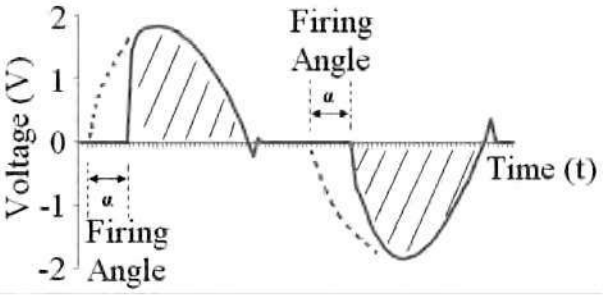

Fig. 4 : Voltage waveform from conditioning circuit

Fig. 5 shows the dynamic resistive pattern that used to predict the process resistance for good against poor weld joints. So the entire dynamic resistive patterns are computed based on this referencing model using current and voltage waveform of 75 kVA spot welder.

When consider the regions (1, 2, 3, 4 and 5) of **Fig. 5**, the region 1 reveals that the impurities on the surface of base metals cause high resistance between electrode tips and metal sheets during the initial current flow and also react as an insulator. As such sharp drop of resistances are found when a proper contact is established between electrode tip and metal sheet. The region 2 exhibits that the contact resistance of base metals is minimized in this region due to the presence of current flow. In another word: the contact areas that have to be welded are well balanced here and it acted as reference point to predict the expulsion states from here on. The calculated value of this region is around 120 μΩ (in part 1). Likewise, the region 3 shows the thermal increment of bulk resistive components (metal resistance) to start the melt process which will initialize the nugget formation between faying surfaces of base metal. The following region is numbered as 4 and it finalises the actual weld diameters. In this region the contact resistance is almost minimized and the

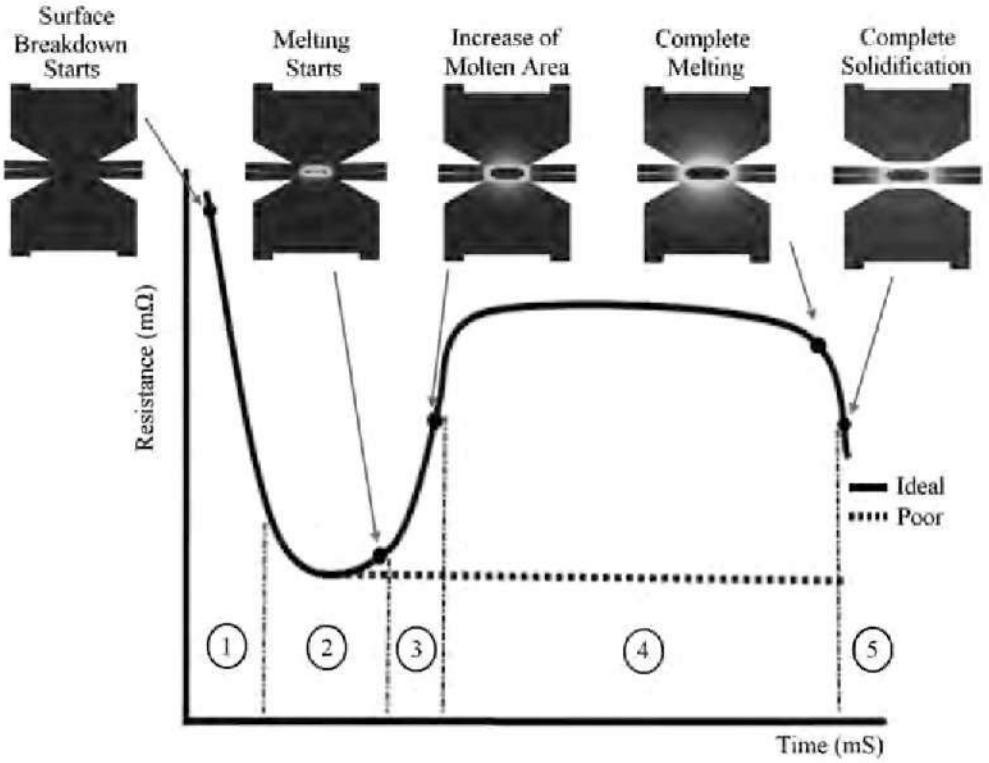

Fig. 5 : Dynamic resistive patterns

temperature seemed to be about constant. Hence the growth of fusion zone (diameter) is clearly noticed in this stage. Furthermore the following region (region 5) does not fall in the welding process but in the solidification process. In this particular stage the liquid metal becomes solid as it known to be the core reason for the macro and micro structural formations. A sharp fall in this region or in the middle of earlier region reveals that an expulsion may have been somewhat occurred. A poor weld joint occurs due to the expulsion as it splashes out the molten metal from the weld nucleus.

Electrically Generated Forging Forces (EGFF) and Maximum Forces

It seems little curious why this effect is called as forging effects at first instance. The answer is simple and straight forward. When the heating and hammering effects are continuously or alternatively applied upon metals in spot welding process, the corresponding effects are thus, as equal as the forging effects in metal forming field. So the term 'forging' refers to a mechanical force variation while heating-up is in progress. According to a review, it defines so far that the mechanically generated forging force is created when the electrode force is purposely escalated (positive forging) or deescalated (negative forging) within the welding lobe's good welds region. Basically, the electrode pressing force can never be constant during welding process because the huge amount of current flow causes total atomic recrystallization of base metals at the fusion zones [8]. If the welding current is sinusoidal waveform, then the directional changes of waveforms cause electrically induced vibration during welding process occurs [9]. Thus, if the welding time is 10 cycles, then there will be 20 directional changes of phases occur during the welding process. These directional changes of huge amount of current flow will generate forging force effects at the area of concentration and concurrently coexist in the force profile. This phenomenon will be called as the electrically generated forging force, from hereon. These electrically generated forging forces seem to be an ascending sinusoidal waveform which has escalated the force levels during welding process. It has been graphically shown in **Fig. 6**.

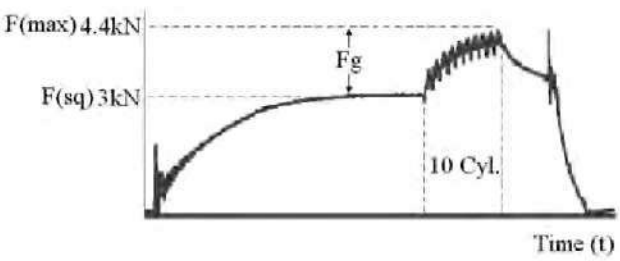

Fig. 6 : Force profiles for the austenitic stainless steel

The electrically generated forging forces (EGFFs) are directly proportional to the welding current, welding time and squeezing forces for constant tip diameter. So it can be mathematically written as; $F_{(Forging)}$, $F_g \alpha I$; $F_g \alpha t$; $F_g \alpha F_{(Squeezed)}$. Let the K1 be the proportional factor of welding current; k2 be the proportional factor of welding time andk3 be the proportional factor of squeezing forces. This mathematical computation leads the way to the final force changing calculation as follows :

Forging Force, $Fg = k1\,(1) \bullet k2(t) \bullet k3\,(F_{(Squeezed)})$

$$Fg = k\,(1tF_{(Squeezed)}) \text{ (where } k = k1 \bullet k2(t) \bullet k3$$

Maximum Force, $F_{(max)} = F_{(Squeezed)}) + F_g$

$$= F_{(Squeezed)}) + k\,(1tF_{(squeezed)})$$

Where F_g is the electrically generated forging force in Newton; $F_{(Squeezed)}$ is the pressing force of electrode in Newton; $F_{(max)}$ is the maximum force in Newton; I is the welding current in Ampere; t is the welding time in Second and k is the proportional factor as dimensionless. Since we have recorded the force profiles for welding processes by using force sensor, the computation becomes straight forward. The proportional coefficient ($k = F_g/ItF_{(Squeezed)}$) of austenitic stainless steel (1 mm thickness) for various level of welding current, welding time and electrode force are measured from the force profiles during welding processes as shown in **Figures 7, 8, 9, 10, 11** and **12.** The forging states are marked by colour circles with capital letters placed inside. These electrically generated forging forces always vary from one machine to another yet, based on its electrode actuation system [10, 11].

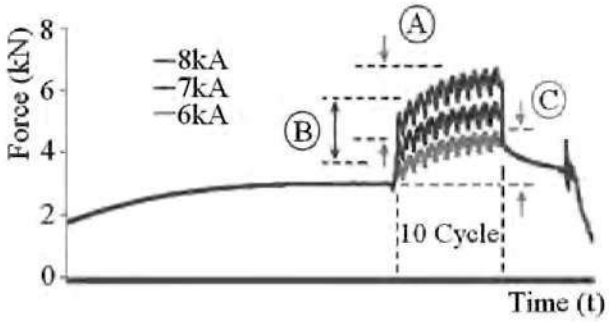

Fig. 7 : Coexistances of EGFFs in force profiles for various current levels (10 cycle)

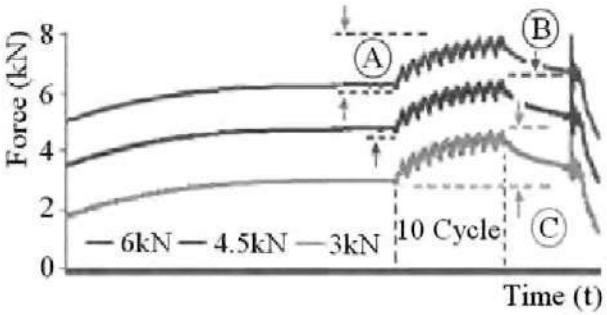

Fig. 8 : Coexistances of EGFFs in force profiles for various force levels (10 cycle)

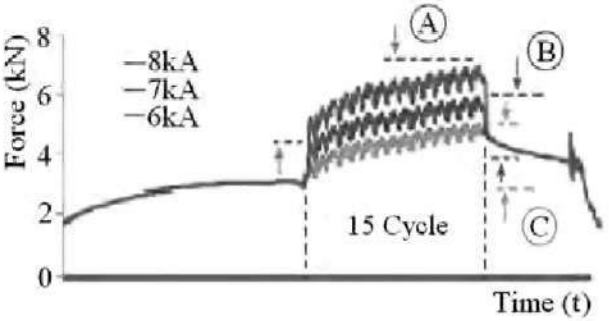

Fig. 9 : Coexistances of EGFFs in force profiles for various current levels (15 cycle)

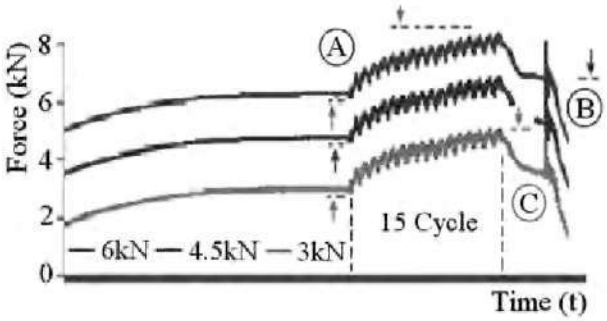

Fig. 10 : Coexistances of EGFFs in force profiles for various force levels (15 cycle)

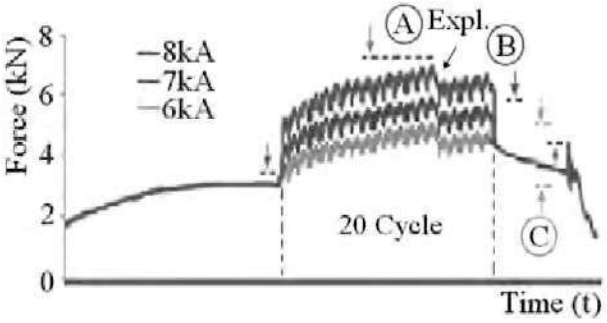

Fig. 11 : Coexistances of EGFFs in force profiles for various current levels (20 cycle)

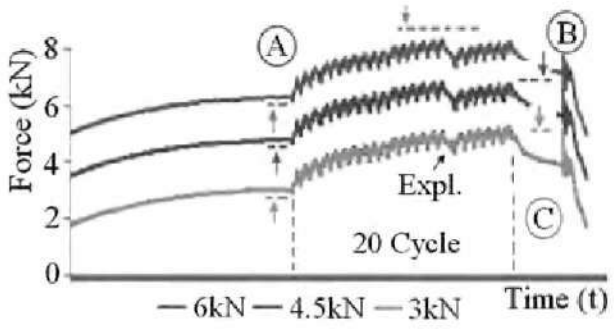

Fig. 12 : Coexistances of EGFFs in force profiles for various force levels (20 cycle)

When analyzing the force profiles that shown above for the 75 kVA pneumatic driven spot welder, the forging forces during welding process seemed to be increasing as the basic controlling parameters (welding current, welding time and electrode force) are increased (**Fig. 13**). Moreover the light expulsion mark is also printed on the force profiles when the welding time is increased beyond its maximum level. Based on these force profiles, the proportional coefficients are calculated which was already listed in **Table 1**.

Dynamic Resistance

Computing the dynamic resistive pattern explains how well the heat ($Q= kI^2Rt$) diffusion has taken place because the resistive component is what ultimately varied while the welding process is going on [12, 13]. Assume that the heat losing factor is common to all the welding processes and therefore can be eliminated this factor 'k' for time being. So the heat formula is now rewritten as $Q=I^2Rt$; and the resistance varies as the welding process goes on. As such the average resistance is calculated as:

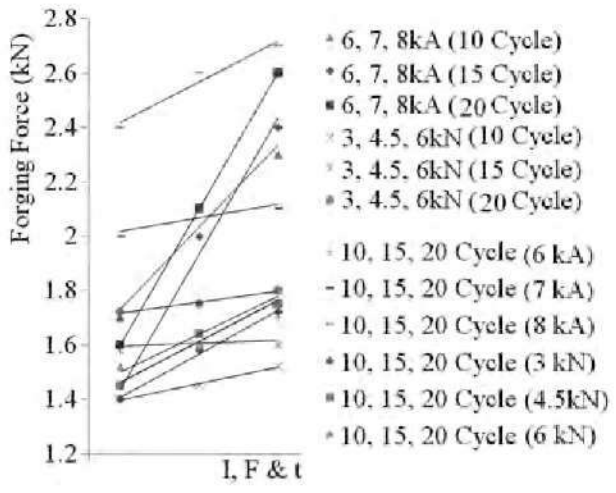

Fig. 13 : Proportionality factors (coefficients) of electrically generated forging forces for 5 mm electrode tip diameter (pneumatic based system)

Average Resistance, $R_{(ave)} = \frac{1}{2N} \sum_{j=1}^{2N} Rj$; where j is the number of the half cycle and N is the total number of weld cycle

Practically the welding current and electrode terminal voltage waveforms are captured for peak levels and also conditioned for root mean square values (multiplying with a factor of $1/\sqrt{2}$) before the calculation for dynamic resistance (R=V/I) is performed. **Fig. 7** shows the force profiles for various current levels when the squeezed force is 3 kN and welding time is 10 weld cycle. The corresponding dynamic resistance for **Fig. 7** is shown in **Fig. 14.** By referring the figure 5 for dynamic resistance model, the **Fig. 14** is seemed to have poor resistive curve. Specifically the regions 1 and 2 seemed to be similar for the referencing model (**Fig. 5**) but the consecutive regions 4 and 5 seemed to be generating a poor flow. This is mainly happened due to the electrically generated forging forces that influence the dynamic resistances. Thus, when the current is increased from 6 to 7 and 7 to 8 kA; the resistive patterns are reduced from one another but the welding current is highly increased. So the average resistances vary as compare to one another. Similarly, the resistive pattern reductions are found for the electrode force increment but there is no increment in welding current such as shown in **Fig. 15**. Literally the welding current and the dynamic resistive patterns are inversely proportional to each other ($R \alpha 1/I$). Likewise, the dynamic resistive patterns are inversely proportional to force ($R \alpha 1/F$) for a given welding time. So these relationship can be written as dynamic resistance, $R = k'/IF$; where k' is the proportional factor of current and force with respect to the dynamic resistance.

Furthermore the dynamic resistive pattern were also computed for 15 and 20 cycles of weld time as shown in figures 16, 17, 18, 19 and 20 respectively. The relationship between welding current, electrode force and dynamic resistance are remained same as before. However the average resistances have been

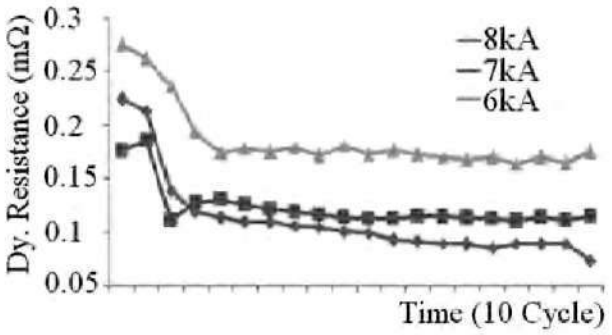

Fig. 14: Variations of dynamic resistances in stainless steel welds for various current levels (10 cycle)

slightly varied as the welding time is increased in such situations. So, based on these average resistance increments, the heat development ($Q=I^2Rt$) for the entire welding process is plotted in **Fig. 7(h)** for comparison purpose. It should be noted from **Fig. 20** that: when the welding current and welding time are increased; the heat distribution is also corespondingly increased. However when the force is increased regardless of welding time increment, the heat distribution is decreased; resulting shorter weld bead formation. Moreover, a very light expulsion is noticed when the welding time reaches the border of welding lobe [14, 15]. This light expulsion causes some voids to be existed at the fusion zone and results poor strength obviously. Finally the heat development graph for parametric changes is tally with the diameter increments and the tensile strength increments graphs which was presented in part 1 of this research.

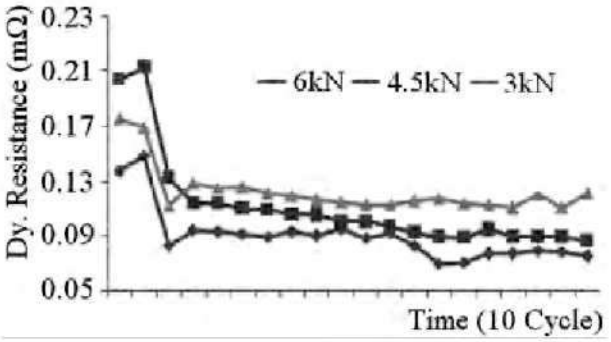

Fig. 15: Variations of dynamic resistances in stainless steel welds for various force levels (10 cycle)

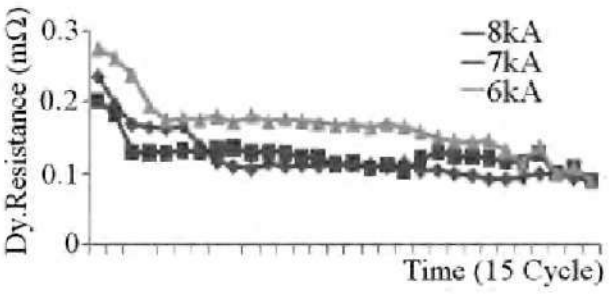

Fig. 16: Variations of dynamic resistances in stainless steel welds for various current levels (15 cycle)

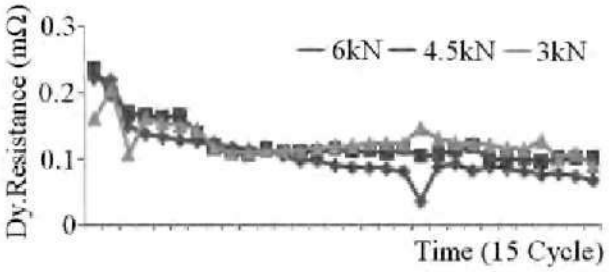

Fig. 17 : Variations of dynamic resistances in stainless steel welds for various force levels (15 cycle)

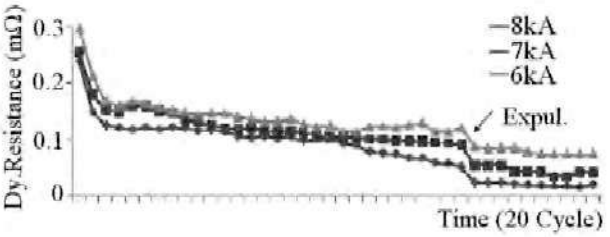

Fig. 18 : Variations of dynamic resistances in stainless steel welds for various current levels (20 cycle)

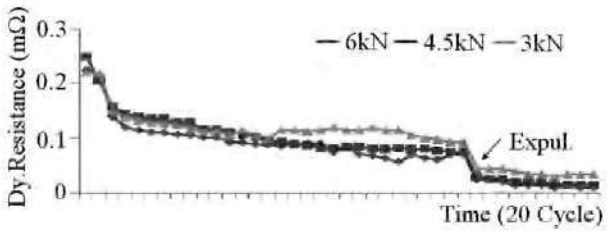

Fig. 19 : Variations of dynamic resistances in stainless steel welds for various force levels (20 cycle)

Metallurgical Study

The metallurgical test was conducted to observe the macro-graphs in relation to the micro structural orientations [16]. This test draws a relationship between poor nuggets against good ones as to predict the exact size of fusion zones, heat affected zones, and the non-molten zones [17]. Part 1 of this research has already discussed the weld diameters as well as the electrode indentation for the equivalent parametric changes. Nevertheless some macro graphs from part 1 have been shown in this paper as to recall the outlook of fusion zones, heat affected zones and the base zones of 304L austenitic stainless steels; so look at the **Fig. 22** for a good weld against a poor weld bead.

The phase properties of stainless steels have been slightly altered due to the solidification process and therefore the ferritic orientation seemed to be shuffled at the weld nucleus. Generally, the solidification of the austenitic steel welds cause minor changes in the dendrites arrangement or sometime in recrystallization. In pneumatic based electrode actuating system, the primary austenitic dendrites and inter-dendrites of ferrite are parallel to the current flow at the welded nucleus. The entire weld nucleus is now seen as recrystallized austenites, surrounded with thin ferrites. Compare the **Figs. 21** and **22** for the micro structural view of unwelded and welded areas, respectively. This phase changes is actually the root cause of very slight increment of hardness in austenitic stainless steel as it has transformed in phases which lead to slight increment of hardness at the welded areas as Rockwell

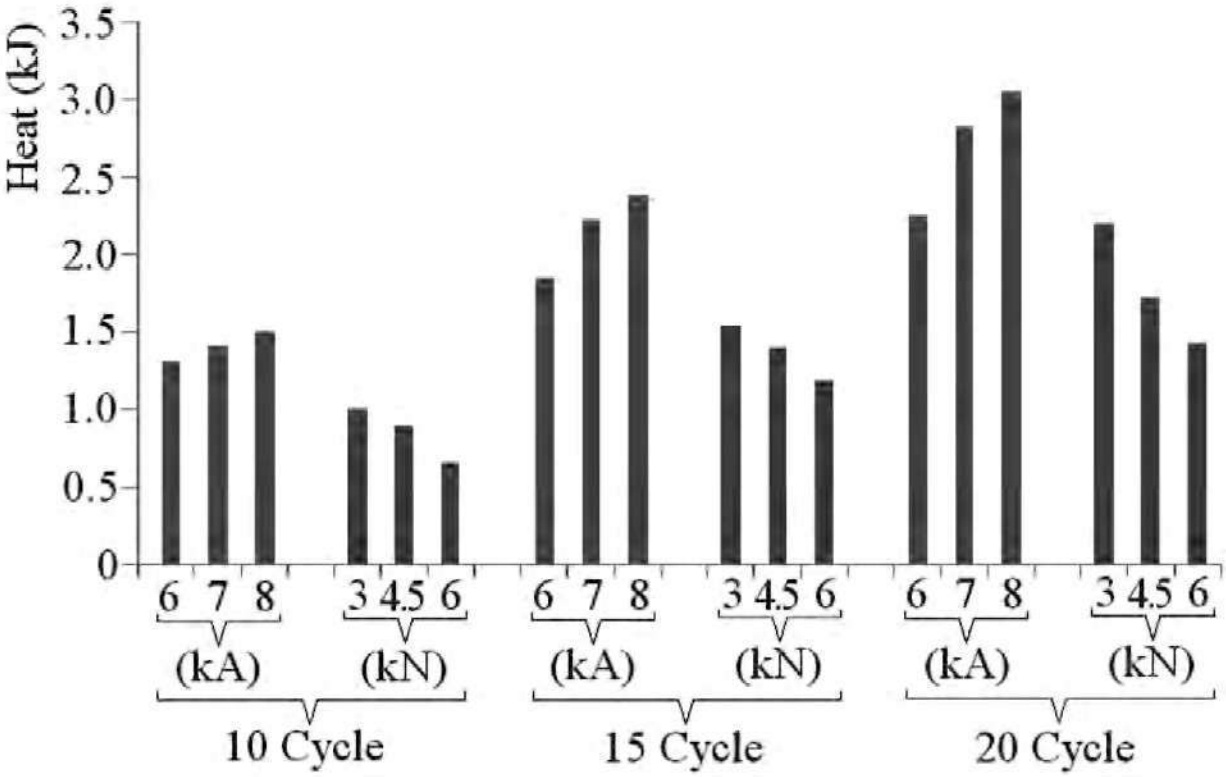

Fig. 20 : Heat development based on the average dynamic resistance

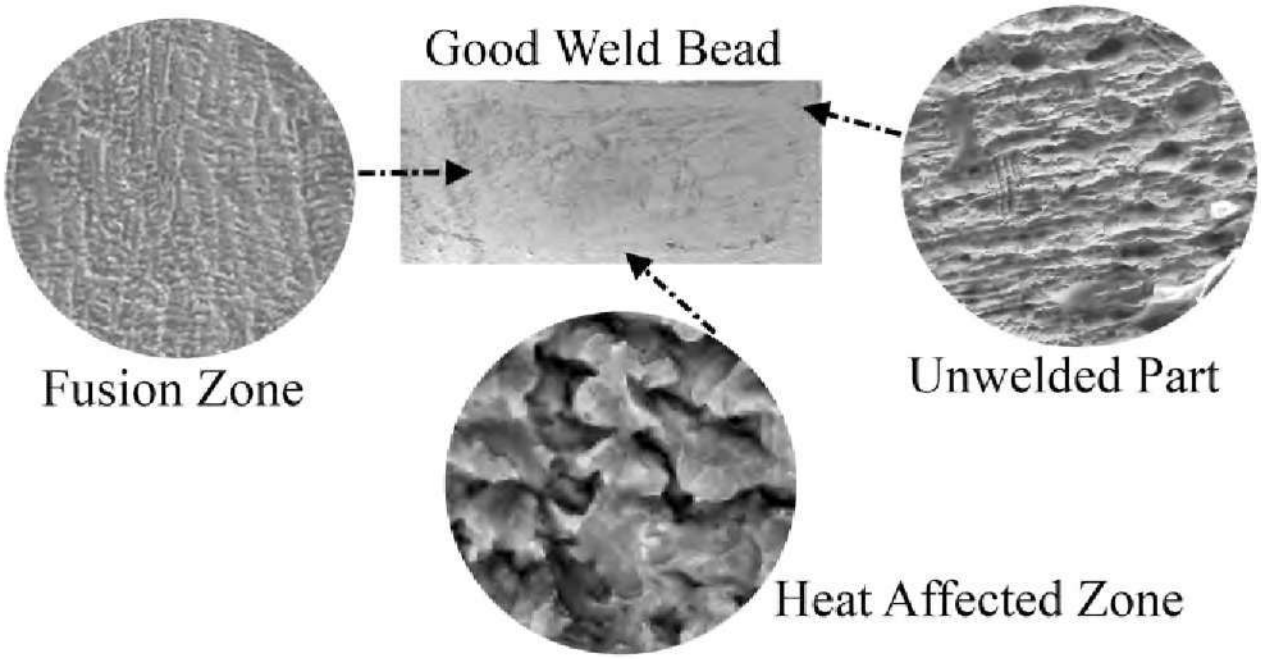

Fig. 21 : Macrograph of a goodly-formed weld bead

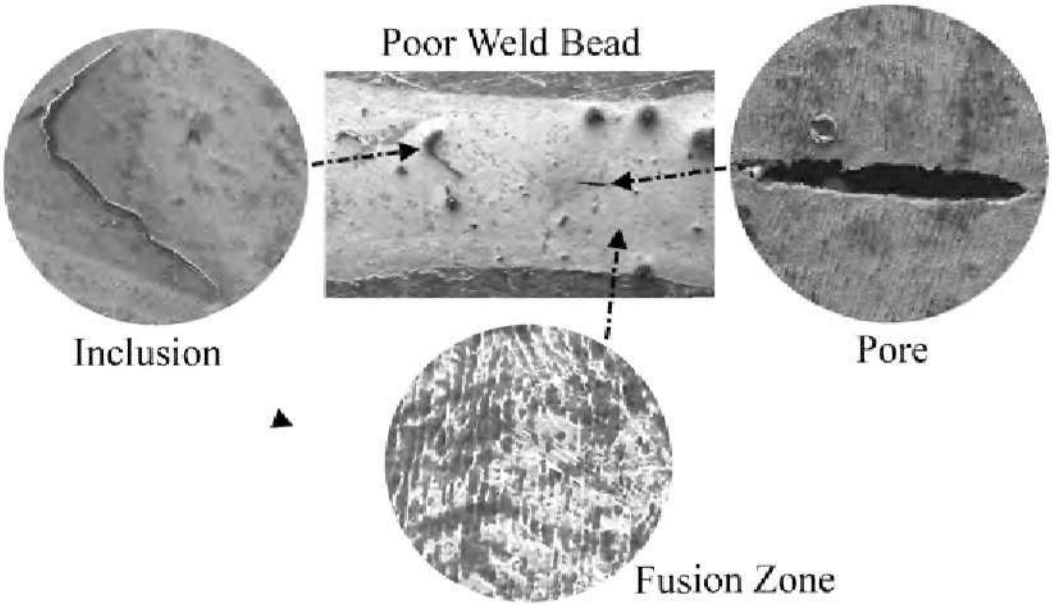

Fig. 22 : Macrograph of a poorly-formed weld bead

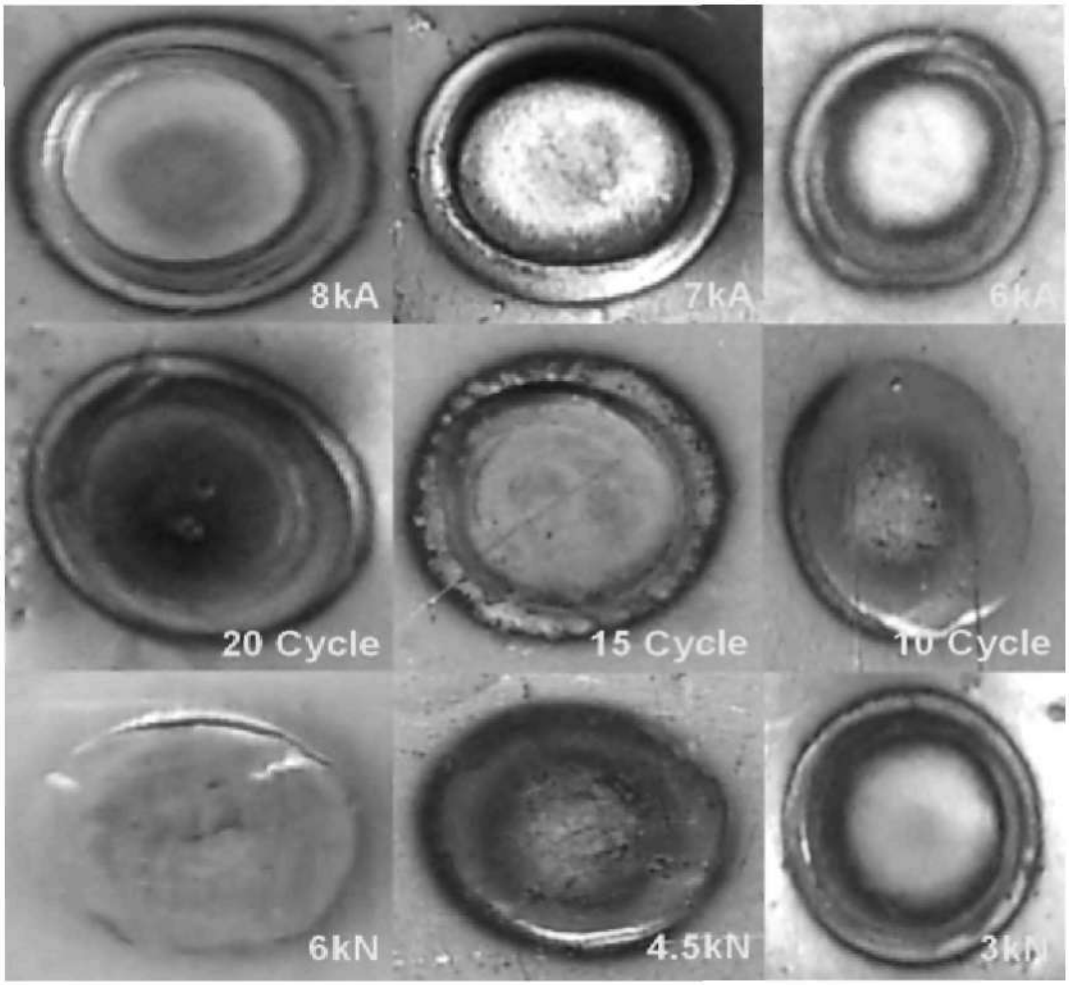

Fig. 23 : Macrograph of weld indentation thst has color circles

hardness proves these increments as well. Let's analyse the heat affected zone as it is seen with multiple-coloured circles or multiple-coloured oval shape printed at the outer and inner regions of welded areas; look at the **Figs. 23** and **24.** From one of the outer most circles, the inner most regions' line exhibits dark blue colour (≈600°C) whereas the outer most line shows pale yellow colour (≈290°C). So the colour contours are drawn for scale and it has been shown in **Fig. 24.** This happens because of the lower thermal conductivity rate of stainless steel. The colour contours are not depicted throughout the weld indentation but just on the surface of welded areas and thereby they are easily erased when undergo any of etching process.

Hardness Test Result

The hardness is an essential parameter to measure because the base metal is completely melted and underwent solidification process during nuggets formation [18]. So it has to be analyzed for the hardness properties at the fusion and also at the heat affected zones [19]. **Fig. 25** shows the hardness comparison between real weld and a simulation work using Visual Basic.

Thus, the fusion zones (FZ) have produced symmetrical views of nugget growth and oval shape in overall is appeared as shown in **Fig. 25**. It has been slightly hardened by the solidification process (phase changes) and the molten areas are directly related to the thermal expansion's coefficient rate (17.2×10^{-6} K^{-1}) of stainless steel. The heat affected zones' (HAZ) hardness is slightly lower than the fusion zone but higher than the base metals. However the oval shape of heat affected zones is noticed because of the truncated electrodes tips and also the thermal conductivity coefficient rate (16.2 W $m^{-1}K^{-1}$) of stainless steel [20, 21]. The hardness of unwelded areas (BM) is approximately 81.7 HRB. As for the welded areas (fusion zones), the hardness is increased to be around 95 HRB and for heat affected zones it is about 87 HRB approximately. These values are more or less same for both categories; as the welding current versus welding time (**Fig. 26**) and welding current versus electrode force (**Fig. 27**).

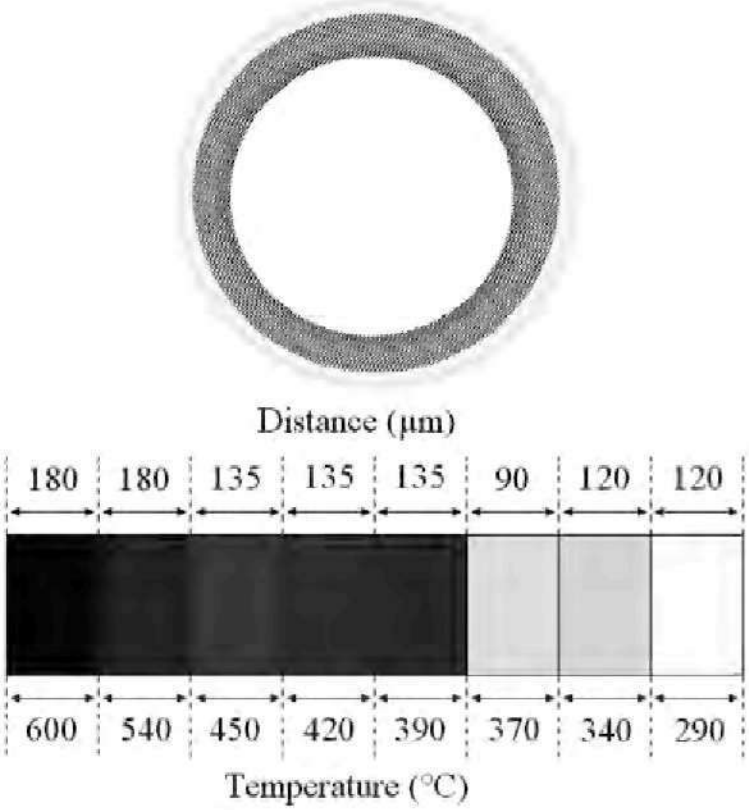

Fig. 24 : Colour contours of heat affected zone

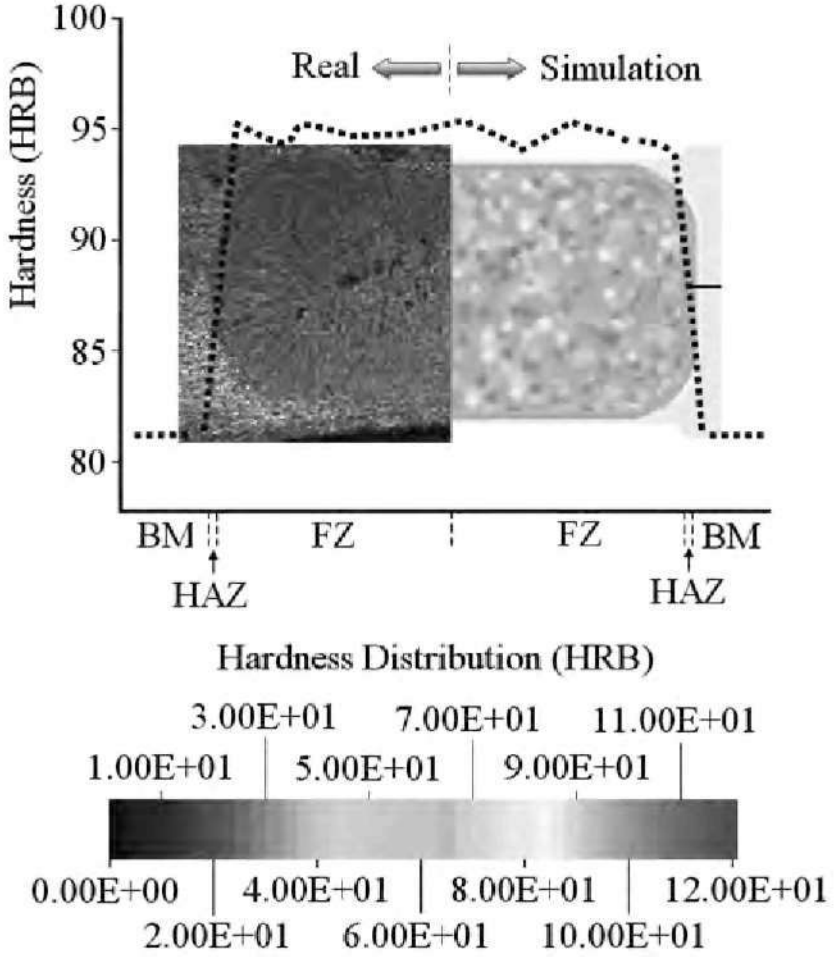

Fig. 25 : Hardness of Austenitic Stainless Steels (weld schedule 1-9)

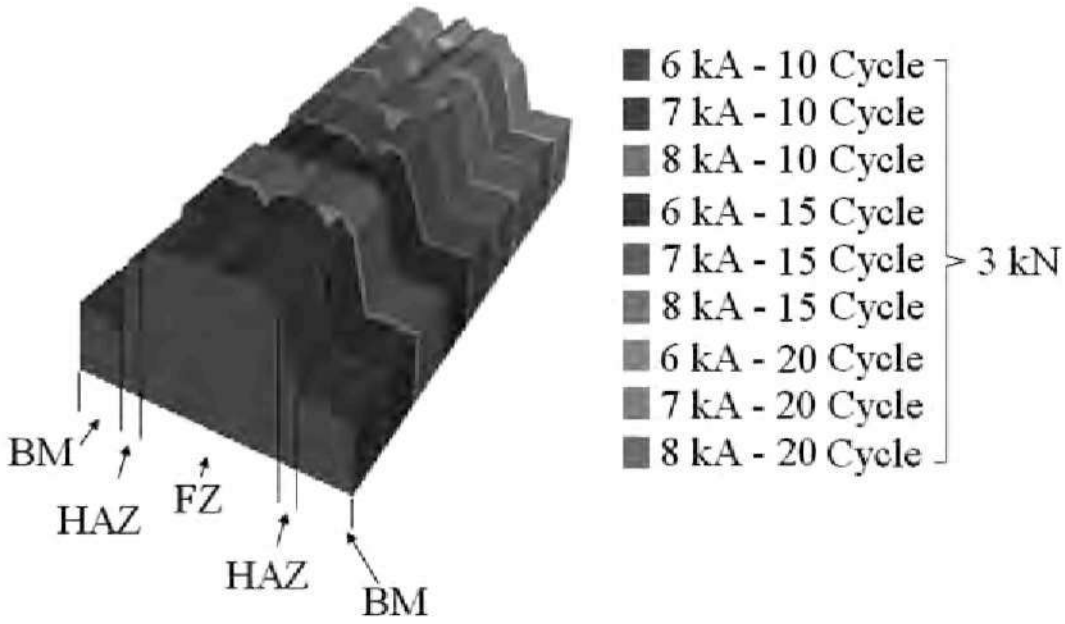

Fig. 26 : Hardness of stainless steel (welding current against welding time category)

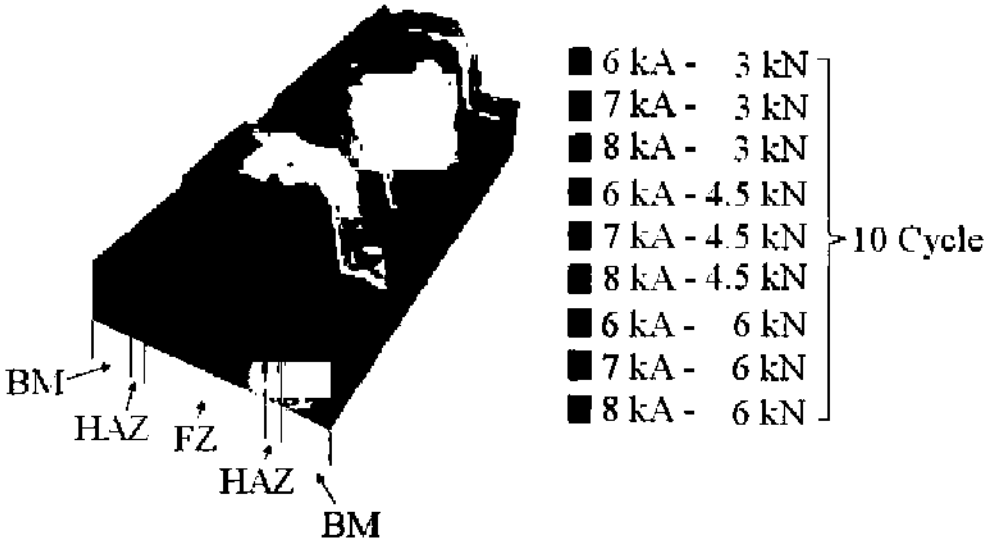

Fig. 27 : Hardness of stainless steel (welding current against electrode force category)

CONCLUSION

This paper looks into the spot welds growth on austenitic stainless steel with 1 mm thickness sheets and it concludes that:

1. Increase in welding current, welding time and electrode force are proportionally increased the electrically generated forging forces within the welding lobe range for 1 mm thickness.
2. Forging force of pneumatic driven spot welder is calculated by $F_g = k(ItF_{(Squeeze)})$; where k (k= k1•k2•k3) is the overall proportional factor of welding current, welding time and electrode force for constant electrode tips.
3. The welding current and electrode force are inversely proportional to dynamic resistive patterns ($R \alpha 1/1F$).
4. The dynamic resistive patterns are slightly differed in this experiment because of the electrically generated forging forces effects. High forging forces lead to poor welding processes as far as the dynamic resistive patterns are referred.
5. The heat development is proportional to the welding current and welding time but inversely proportional to electrode force.
6. Micro structures exhibit the coarsened grains at fusion zone and unchanged grains at base metal; clearly.
7. The hardness values of welded areas are seemingly increased (From 81.7 to 95 HRB in average) due to the phase transition.
8. The increase in welding current or welding time or electrode force does not influence the hardness distribution along the welded areas.

ACKNOWLEDGEMENTS:

I would like to thank the University Malaya, Malaysia for its assistance in preparing this paper. This research outcome is part of Nachimani's doctoral research work.

REFERENCES

[1] Nachimani C. 2014. Resistance spot welds of 304l austenitic stainless steel, part 1: fundamental, simulation, weld growth, tensile strength and failure mode analysis. Indian Welding Journal, Volume 48, 1-14.

[2] Chang BH, Du D and Sui B. 2006. Effect of forging force on fatigue behavior of spot welded joints of aluminum alloy 5182. Journal of Manufacturing Science and Engineering, 345-352.

[3] Nachimani C. 2012a. Effects of electrode deformation on 304 austenitic stainless steel weld geometry of resistance spot welding. Journal of Mechanical Engineering and Sciences, Volume 3, 261-270.

[4] Nachimani C. 2012b. Spot weld growth on 304L austenitic stainless steel for equal and unequal thicknesses. Caspian Journal of Applied Sciences Research, Volume 1(11), 79-87.

[5] Guocheng X, Ling WC, Sheng Wang and Xiaoqi Zhang 2009. Quality monitoring for resistance spot welding using dynamic signals. Proceedings of the IEEE International Conference on Mechatronics and Automation, 456-462.

[6] Shih. 2010. Input electrical impedance as quality monitoring signature for characterizing resistance spot welding. NDT&E International, Volume 43, 200-205.

[7] Cullen JD, Wong S. and Chow SW. 2011. Multi sensor spot welding monitors using wireless sensor network technology. IEEE Symposium on Computers & Informatics.

[8] Tang H, Hou W and Hu SJ. 2002. Forging force in resistance spot welding. Proceedings of the Institution of Mechanical Engineers, Part B: Journal of Engineering Manufacture, Volume 216, 957-965.

[9] Rinsei I, Yasuaki O, Moriaki O, Koichi Y and Toshio T. 2006. Development of advanced resistance spot welding process using control of electrode force and welding current during welding. Journal of the Japan Welding Society, Volume 28(1), 141-148.

[10] Zhang YS, Wang H, Chen GL and Zhang XQ. 2007. Monitoring and intelligent control of electrode wear based on a measured electrode displacement curve in resistance spot welding. Measurement Science and Technology, Volume 18, 867-876.

[11] Isaev AP. 2006. A method for modeling the pneumatic drive and load carrying structure of resistance spot welding machines. Svarochnoe Proizvodstvo, Volume 59(3), 18-25.

[12] Tang H, Hou W, Hu SJ, Zhang HY, Feng Z, and Kimchi M. 2003. Influence of welding machine mechanical characteristics on the resistance spot welding process and weld quality. Welding Journal, 133s-140s.

[13] Senkara J, Zhang H, and Hu SJ. 2004. Expulsion prediction in resistance spot welding. Welding Journal, 120s-128s.

[14] Dancette S, Fabregue D, Massardier V, Merlin J, Dupuy T and Bouzekri M. 2012. Investigation of the tensile shear fracture of advanced high strength steel spot welds. Engineering Failure Analysis, Volume 25, 112-122.

[15] Hong GY. 2010. Investigations on sheet to cylindrical tube single-sided spot welding using servo gun. Proceedings of the International Conference on Computer Mechatronic Control and Electronic Engineering, 166-172.

[16] Inoue AH. 1997. Solidification and transformation behaviour of austenitic stainless steel weld metals solidified as primary ferrite: study of solidification and subsequent transformation of Cr-Ni stainless steel weld metals. Journal of the Japan Welding Society, Volume 1.5(I), 88-99.

[17] Haraprasanna T. 2013. Thermal stability and thermal property characterisation of Fe–14.4 Cr–15.4 Ni–2.4 Mo–2.36 Mn–0.25 Ti–1.02 Si–0.042 C–0.04 P–0.005 B austenitic stainless steel (Alloy D9I). Nuclear Engineering and Design, Volume 255, 86- 96.

[18] Spinelli JE. 2004. Microstructure and solidification thermal parameters in thin strip continuous casting of a stainless steel. Journal of Materials Processing Technology, Volume 150, 255-262.

[19] Huang FX. 2008. In situ observation of solidification process of AISI 304 austenitic stainless steel. Journal of Iron and Steel Research, Volume 15(6), 78-82.

[20] Jamasri T, Ilman MN and Soekrisno R. 2009. Comparative study of fatigue assessment methods with and without considering residual stress on resistance spot-welded unequal sheet thickness stainless steel. International Journal of Engineering & Technology, Volume 11, 456-462.

[21] Pouranvari M and Marashib SPH. 2010. Failure mode transition in AHSS resistance spot welds, Part I: Controlling factors. Materials Science and Engineering A, Volume 528, 8337-8343.